Resonant Controllers with Three-Degree of Freedom for AC Power Electronic Converters

Alessandro Lidozzi, Luca Solero,
Fabio Crescimbini

Department of Engineering
Roma Tre University
Roma, Italy. alessandro.lidozzi@uniroma3.it

Marco Di Benedetto, Stefano Bifaretti

Department of Industrial Engineering
University of Rome Tor Vergata
Roma, Italy. bifaretti@ing.uniroma2.it

Abstract – **Grid-connected and stand-alone applications need inverters that accurately control the filter output voltages. Nowadays, resonant controllers represent a good tradeoff between implementation issues and control performances. However, the unknown nature and size of supplied loads affect the dynamic control behavior and may reduce the effectiveness of the control system. A new structure of resonant controller is introduced with the purpose to provide three-degree of freedom and allowing to select independently the controller's magnitude, width and phase. In order to fully take advantage of the proposed resonant controller form, the on-line tuning procedure based on the output filter analysis is also proposed. According to that, several resonant compensators can be placed in the loop to achieve better output voltage waveform, (i.e. lower total harmonic distortion).**

Index Terms – **Adaptive tuning, phase compensation, resonant controller, voltage source inverter.**

I. INTRODUCTION

Resonant Controllers (RCs), which are derived from the internal model principle [1], are today applied in several fields, such as static power conversion for both grid-tied and stand-alone applications, high performance control of electric drive and renewable energy systems [2]-[6]. Conventional resonant controller forms are well explained and widely applied as in [7]-[9] even in case of unbalanced linear and non-linear loads [10]-[12].

Analysis and design of proportional-resonant control structure with the aid of Nyquist diagrams for current controlled VSI is depicted in [13]; in that case the tuning process does not include how the load could affect the system stability.

RC phase compensation capabilities were preliminary discussed in [14]; however, RC ideal representation and application to a single phase inverter, with control algorithm tuned in a specific stationary point, were considered. An ideal RC provides infinite gain at the resonance frequency without the ability to select the controller width. Moreover, discretization issues arise especially when controllers are implemented on industrial grade Digital Signal Processors (DSPs) or microcontrollers (μCs) with limited computational capabilities [15]-[17].

The proposed paper introduces the full non-ideal RC with phase compensation capabilities, which is denoted as 3-Degree of freedom Resonant Controller (3D-RC) allowing extra flexibility in control parameters tuning and superior regulation performances.

The 3D-RC is then applied, in the multi-resonant controller structure, to a three-phase four-leg VSI which operates in islanding mode [10]-[11], for both output voltage regulation and harmonic compensation when non-linear loads have to be fed. The newly introduced 3D-RC is able to provide the necessary magnitude and phase boost to compensate for the inverter output power filter behavior according to the operating conditions. As it is shown in the following, passive filtering used to attenuate the switching ripple introduces a quite limited magnitude variations and strong phase lagging effects; in fact, the filter per unit delay increases with the harmonic order to be compensated through RCs.

II. THREE-DEGREE OF FREEDOM RESONANT CONTROLLER

In order to introduce the 3D-RC, the non-ideal full form of the RC has been selected, as it is the most versatile and suitable to be implemented in the final digital form. The transfer function G_{RC2} of the non-ideal controller

$$G_{RC2}(s) = 2k_{ir}\omega_{cr}\frac{s+\omega_{cr}}{s^2+2\omega_{cr}s+\left(\omega_{cr}^2+\omega_0^2\right)} \quad (1)$$

where k_{ir} is the controller gain, ω_{cr} the controller width and ω_0 the resonance frequency, is able to provide the necessary gain in order to reach zero steady-state error, still allowing the regulation of the controller width. Non-ideal RCs exhibit two degrees of freedom providing the capability to regulate, almost independently, both the controller gain and width.

In this form, even if it is possible to control both the gain and the width of the RC, controller phase is locked to be 0° at the resonance frequency and cannot be used as a design parameter. In order to introduce the possibility to select the controller phase at the resonant frequency, the RC structure needs to be modified as follows.

Complete phase control can be achieved by adding two terms to the non-ideal form in (1), both related to the desired angle ϑ at the resonant frequency, as in (2). This angle is the phase boost that will be provided by the RC and selected according to the control requirements.

$$G_{RC3}(s) = 2k_{ir}\omega_{cr}\frac{s\cos(\vartheta)+\omega_{cr}-\omega_0\sin(\vartheta)}{s^2+2\omega_{cr}s+\left(\omega_{cr}^2+\omega_0^2\right)} \quad (2)$$

A. Controller phase

Controller phase can be evaluated considering numerator and denominator separately as in:

$$N_{RC3}(s) = 2k_{ir}\omega_{cr}\left[s\cos(\vartheta)+\omega_{cr}-\omega_0\sin(\vartheta)\right]$$

$$D_{RC3}(s) = s^2+2\omega_{cr}s+\left(\omega_{cr}^2+\omega_0^2\right) \quad (3)$$

Complete expression for the RC phase is calculated according to (4).

$$\varphi_{RC3} = \angle N_{RC3}(s) - \angle D_{RC3}(s) \qquad (4)$$

Substituting $s=j\omega$, the final expressions for the resonant controller angle are:

$$\angle N_{RC3}(j\omega) = \operatorname{atan}\left(\frac{\omega\cos(\vartheta)}{\omega_{cr} - \omega_0\sin(\vartheta)}\right) \qquad (5)$$

$$\angle D_{RC3}(j\omega) = \operatorname{atan}\left(\frac{2\omega\omega_{cr}}{\omega_{cr}^2 + \omega_0^2 - \omega^2}\right) \qquad (6)$$

For evaluation purpose, previously shown equations should be considered, taking into account that $\omega_{cr} \ll \omega_0$ is usually verified for common grid-tied and stand-alone applications. Moreover, as the order of the resonant controller increases, its width ω_{cr} is usually reduced to guarantee the overall system stability. Eqs. (5) and (6) can be plotted to show the behavior of numerator and denominator phase vs. frequency for a given angle ϑ. Fig. 1 is obtained with $\omega_{cr}=0.003$ rad/s and $\omega_0 \approx 314$ rad/s. The dashed line is related to the denominator's phase, while numerator's phase is shown with solid lines and plotted at four values of the angle ϑ: $-\pi/6$, 0, $\pi/6$ and $\pi/3$. As it can be verified in Fig. 1, the numerator's phase at the resonance frequency can be written as:

$$\left.\angle N_{RC3}(s)\right|_{s=j\omega_0} = \frac{\pi}{2} + \vartheta \qquad (7)$$

where ϑ is the desired controller phase at the selected resonance frequency. With reference to the denominator, its phase contribution can be summarized as in (8).

$$\begin{cases} \left.\angle D_{RC3}(j\omega)\right|_{\omega \ll \omega_0} \approx 0 \\ \left.\angle D_{RC3}(j\omega)\right|_{\omega = \omega_0} \approx \pi/2 \\ \left.\angle D_{RC3}(j\omega)\right|_{\omega \gg \omega_0} \approx \pi \end{cases} \qquad (8)$$
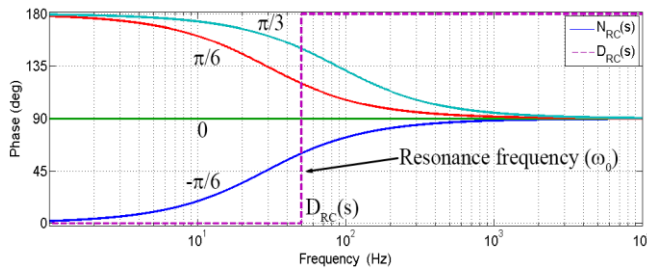

Fig. 1. Numerator and denominator phase of the real harmonic controller for different values of the angle ϑ.

Hence, the phase shown in (4) when calculated at the resonance frequency yields

$$\varphi_{RC3} = \underbrace{\vartheta + \frac{\pi}{2}}_{\angle N_{RC3}} - \underbrace{\frac{\pi}{2}}_{\angle D_{RC3}} = \vartheta \qquad (9)$$

This proves the effectiveness of the phase control extended to the full form of the resonant controller. From (9) it can be noticed that RC phase at the resonance frequency is weakly affected by the selected value of the controller width, whereas it does not depend on the controller gain as shown in (5) and (6) for both numerator and denominator. Fig. 2 shows the Bode diagram of (2) for various value of ϑ. However, all these parameters have to be considered for a multiple harmonic control system. In fact, even if this method provides the ability to control the RC phase in order to compensate for the system behavior, it also presents some drawbacks. From Fig. 2 is noticeable how the larger is ϑ, the higher is the asymmetry in the magnitude function of the RC. Looking at the zero-map of the phase-controlled RC, as shown in Fig. 3, it can be seen how the phase disposition only acts on the positioning of the RC transfer function zero. In this figure, the circles are related to the position of the zero for a single RC for different values of ϑ. It can be noticed the modification of the zero from having a positive real part to a negative real part when a phase boost ($\vartheta > 0$) have to be provided.
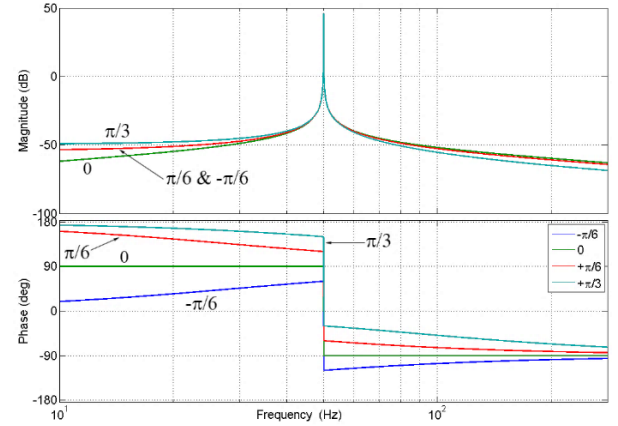

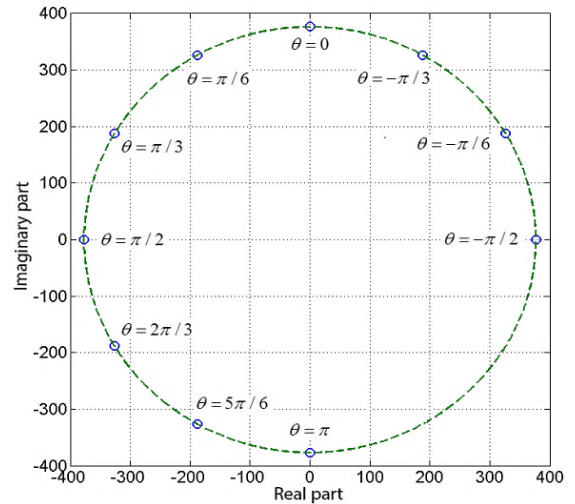Fig. 2. Bode plots for the non-ideal resonant controller for different ϑ.

Fig. 3. Position of the controller zero at the resonance frequency on the complex plane for different values of the angle ϑ.

B. Controller magnitude

Starting from (2), the magnitude function of the RC can be evaluated in a similar way as the one used to demonstrate the phase control capability.

The magnitude at the resonance frequency is expressed as in (10). Usually, in RCs, the width parameter ω_{cr} is selected in the range from tens micro radians per seconds to less than hundreds milliradians per second. Being ω_{cr} smaller than ω_0 and lower than one, (10) can be simplified as in (11).

$$\left|G_{RC3}(j\omega_0)\right| = 2k_{ir}\sqrt{\frac{\omega_{cr}^2 - 2\omega_{cr}\omega_0\sin(\vartheta) + \omega_0^2}{4\omega_0^2 + \omega_{cr}^2}} \quad (10)$$

$$\left|G_{RC3}(j\omega_0)\right| = k_{ir}\sqrt{\frac{-2\omega_{cr}\sin(\vartheta) + \omega_0}{\omega_0}} \quad (11)$$

Expression (11) shows that magnitude is directly affected by the desired amount of phase that need to be compensated. Fig. 4 shows the magnitude (10) plotted versus the controller width ω_{cr} for different values of the angle ϑ.

In stand-alone applications, the output frequency is imposed by the front-end inverter; this allows using narrow RCs (i.e. controllers having a reduced ω_{cr} value). On the contrary, in grid-connected systems, due to the fluctuations of the electrical frequency, it would be better to have wide RCs. However, in both types of application, the RC width is selected usually in the previously mentioned range. Fig. 4 shows how it is possible to approximate the magnitude of the RC with the value of k_{ir} (12), being the error very small ($< 0.1\%$) in the selected ω_{cr} range

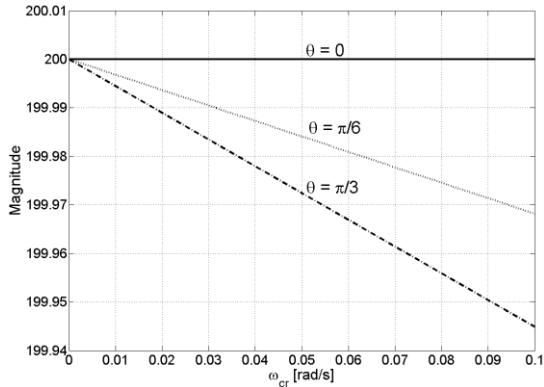$$\left|G_{RC3}(j\omega_0)\right| \approx k_{ir} \quad (12)$$

Fig. 4. Magnitude of the real not-approximated RC at the resonance frequency for different values of ϑ; $k_{ir}=200$, $\omega_0=314$ rad/s.

III. SYSTEM DESCRIPTION, ANALYSIS AND MODELING

The proposed 3D-RC structure is designed and investigated with reference to electric utility applications. Fig. 5 depicts the common structure of a front-end inverter devoted to supply a 3-phase plus neutral stand-alone grid. The common DC-bus can be shared among different power sources as batteries, ultracapacitors, fixed or variable speed generating units, wind energy power systems and photovoltaic arrays. In all these cases, front-end inverter plays an important role being the last interface between sources and grid and/or isolated loads. In such applications, the four-leg VSI must be able to supply different loads such as linear, non-linear, stationary and rotating electrical machines and, of course, a combination of the previously mentioned loads. According to that, control algorithm has to work with a continuous variation of the output power factor, from one (pure resistive load) to very small values (e.g. induction motors running at no-load).

The prototype of a 40 kVA four-leg inverter, shown in Fig. 6, has been built to perform the test and validation campaign. The control unit is based on the TMS320F28335 Digital Signal Controller from Texas Instruments having a dedicated scheduler operating at a frequency of 12 kHz.
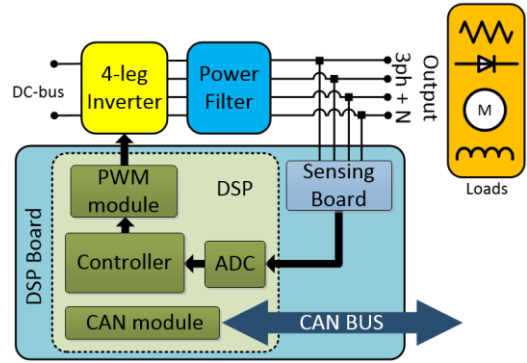

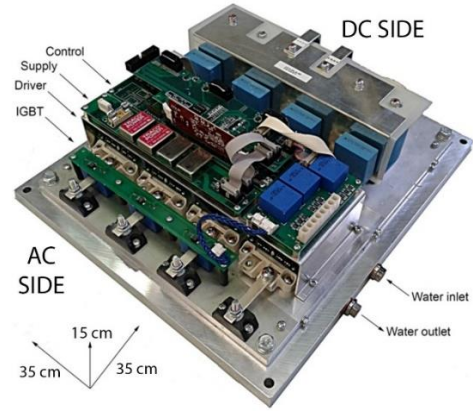Fig. 5. Block scheme of the front-end inverter and related controller.

Fig. 6. Four-leg inverter prototype used for the experimental campaign.

The usage of an inverter output filter is mandatory in order to remove the switching component from the output voltage and current waveforms. Considering the reference application, the implemented single-phase equivalent filter structure is shown in Fig. 7 where a common *LC* second order filter is connected to two tuned RLC branches, the trap-filter and the selective damper [18]. The passive selective damper is centered at a frequency around 1.2 times the *LC* resonance frequency in order to properly damp the main filter resonance peak, making the resistor R_d visible to the rest of the circuit only in a limited range of frequency.

This selectivity behavior drastically shrinks the size of the damper directly reducing the total dissipated power, hence increasing the system efficiency. The switching trap is instead tuned to resonate at the switching frequency in order to short-circuit the fundamental switching component. The element R_t can be considered as the sum of L_t and C_t parasitic resistance. Values of the filter parameters are listed in Table I.

With reference to stand-alone applications, filter magnitude and phase behavior are strongly affected by the actual inverter output power. In fact, modeling the connected loads as an equivalent resistive load (i.e. power factor equal to one), as the supplied power increases, filter results in higher damping and its magnitude and phase behaviors are modified. Fig. 8 shows the output power filter Bode plots at four different output equivalent power levels. It can be noticed how the LC resonance, already influenced by the selective damper circuit, becomes further damped as the output power increases.
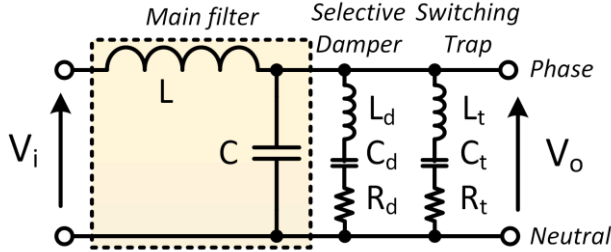
Fig. 7. Scheme of the inverter output power filter.

TABLE I – OUTPUT FILTER PARAMETERS

L_k	800 μH
C_{fl}	5 μF
L_d	1 mH
C_d	2.2 μF + 0.47 μF
R_d	15 Ω
L_t	172 μH
C_t	2 x 0.56 μF
R_t	50 mΩ

Considering the complete system modeling previously depicted in [11], filter behavior at different load conditions can be analyzed by the usage of Bode plots. The effect of the time-lag introduced by the sampling-PWM unit can also be taken into account, when not negligible, by a first order approximation as already shown in [11]. Generating unit load variations are modeled by an equivalent output passive load. A pure resistive load is used to take into account a unitary power factor operation, whereas resistive-reactive equivalent load has been used to test non-unitary power factor. In a multi-resonant control structure, when RCs having an order higher than the fundamental are used, phase effects and magnitude variations become significant, as highlighted in Fig. 8. The proposed 3D-RC structure is able to completely compensate for the described effects allowing a constant-gain constant-phase operation. This particular feature becomes important especially when a low switching

frequency inverter has to be used with low output filter cut-off frequency.

Fig. 9 shows the filter Bode magnitude and phase plots at different output power with a Power Factor (PF) equal to 0.866. It can be noticed how inductive-resistive (L-R) loads do not affect system stability as they lightly influence the complete filter phase and magnitude; on the contrary, as depicted in Fig. 9, the resonance remains almost undamped.
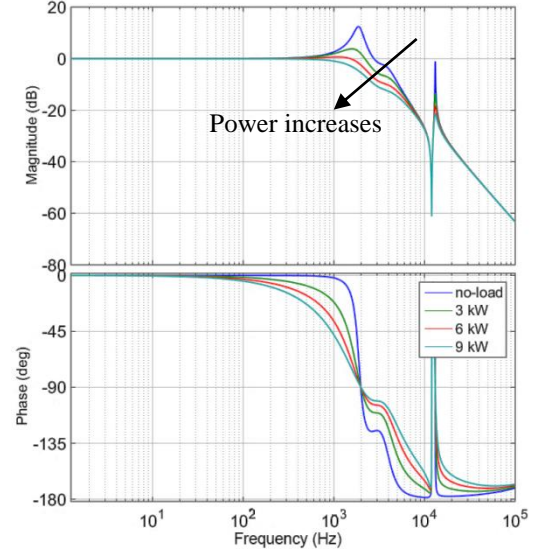
Fig. 8. Bode plots of the equivalent output power filter at different loads, PF=1.
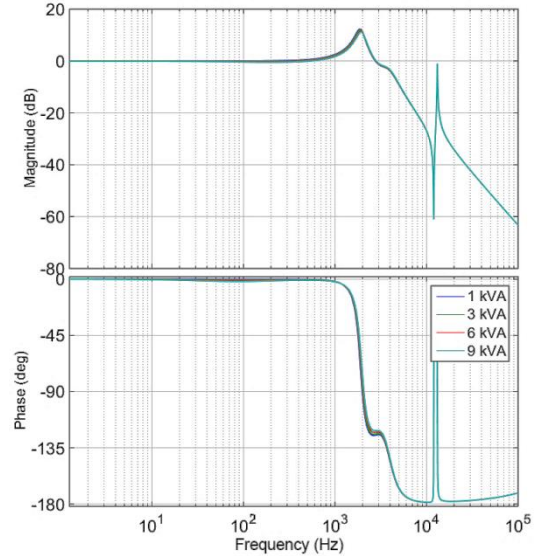
Fig. 9. Bode plots of the equivalent output power filter at different loads, PF=0.866.

According to the previous analysis, magnitude and phase variations due to filter-load interaction are shown in Fig. 10, achieved with reference to each harmonic and as a function of the equivalent output power. For a better readability, only odd harmonics are shown in the range from 15th to 49th. It can be noticed that as the harmonic order increases, a stronger compensation in terms of magnitude and phase is

required. Analytical representation of the behavior shown in Fig. 10 is used to implement the proposed ACS on the Digital Signal Processor.
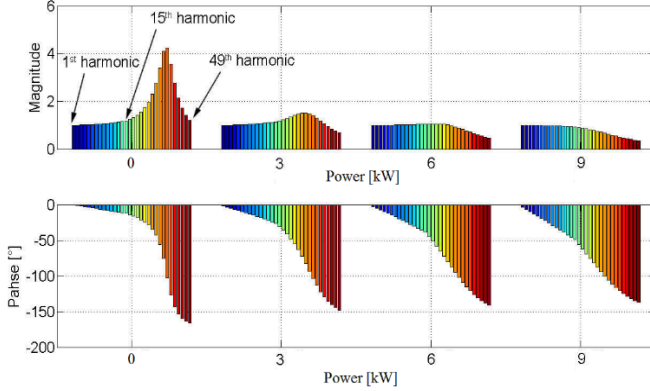

Fig. 10. Filter-load magnitude and phase at different output powers for each RC frequency position.

IV. PROPOSED ADAPTIVE CONTROL STRATEGY

In order to overcome the illustrated drawback introduced by the interaction between the inverter output filter and the loads, an Adaptive Control Structure (ACS) is proposed for this particular application. The ACS is composed by a multi 3D-RC, where each RC is centered at the desired frequency to be regulated. The ACS is able to exploit the benefits of the introduced 3-Degree of freedom Resonant Controllers (3D-RCs) evaluating the correct controllers magnitude and phase.

According to Fig. 11, the block $G_{RC(n)}(s)$ represents the complete transfer function of the multi 3D-RC with phase compensation capability as in (2), it is intended as

$$G_{RC(n)}(s) = G_{RC1}(s) + ... + G_{RC(h)}(s) =$$
$$= \sum_{n=1}^{h} 2k_{ir(n)}\omega_{cr(n)} \frac{s\cos(\vartheta_{(n)}) + \omega_{cr(n)} - \omega_{0(n)}\sin(\vartheta_{(n)})}{s^2 + 2\omega_{cr(n)}s + \left(\omega_{cr(n)}^2 + \omega_{0(n)}^2\right)} \quad (13)$$

where $k_{ir(n)}$, $\vartheta_{(n)}$, $\omega_{cr(n)}$, and $\omega_{0(n)}$ have been illustrated in (1) and (2); h is intended as the maximum harmonic order that is included in the multi 3D-RC. In the following, $M_{RC(1)}...M_{RC(h)}$ and $\theta_{(1)}...\theta_{(h)}$ denote respectively the magnitude and phase of each RC up to the harmonic order h.

VSI is modeled as a gain plus a delay equal to *1.5* times the switching period and it is represented by the following transfer function

$$G_{4-leg}(s) = \frac{K_m V_{dc}}{1 + \frac{1.5}{2\pi F_{sw}}s} \quad (14)$$

where F_{sw} is switching frequency, V_{dc} the inverter DC-link voltage and K_m a gain related to the selected modulation strategy (*0.5* for PWM and *0.57* for SVM or Carrier Based PWM).

In Fig. 11, $G_f(s)$ is the output power filter and equivalent load transfer function. It can be achieved with reference to Fig. 7, evaluating the complete output voltage-to-input

voltage transfer function taking into account the load behavior. It is obtained evaluating the parallel of the impedances related to the selective damper branch, switching trap and load, with the main LC filter [18].

Finally, $G_B(s)$ is a second order low-pass Butterworth type filter having a cutoff frequency set to *10 kHz*. It is used for output voltages measurement. Hence, the resulting transfer function is in the following form

$$G_B(s) = \left(\frac{\omega_f^2}{s^2 + \sqrt{2}\omega_f s + \omega_f^2} \right) \quad (15)$$
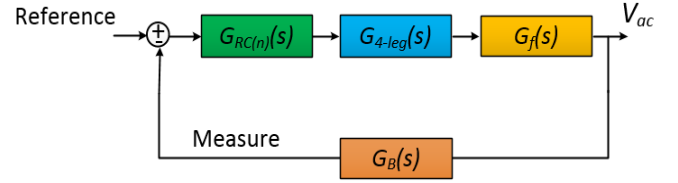
where ω_f is the filter cut-off frequency.

Fig. 11. Block scheme of the inverter control loop.

A specific control algorithm is required to compensate for both filter magnitude and phase variations. To this aim, the tuning strategy requires to know the inverter output operating conditions, which means output power as well as power factor. Moreover, as the supplied loads can be either single-phase or three-phase loads, the control has to regulate the output voltage of each phase independently, thus operating the three-phase four-leg VSI as three totally independent single-phase inverters. The four-leg topology has been selected as it allows controlling the voltage of the neutral connection providing a three-phase balanced voltage system even in case of non-linear and unbalanced loads. In order to adapt the control structure to the load conditions, it is necessary to evaluate the inverter operating point in terms of active (P_{out}) and reactive (Q_{out}) power supplied to the loads. Several algorithms have been proposed so far to calculate instantaneous P and Q power [19]-[21]; however, they all require a significant increase of the computational burden.

Algorithms based on *dq-axes* power calculation should be avoided even if they require low computational effort, being the four-leg inverter devoted to supply both single-phase and three-phase unbalanced loads. For these reasons, it was chosen to employ an off-the-shelf integrated circuit, as the *ADE7953* from Analog Devices. It is able to evaluate the complete active and reactive power demanded to the loads.

Complete ACS block diagram, which is able to compensate both filter magnitude and phase variations, is shown in Fig. 12. The *Load & PF Estimation* block continuously performs the evaluation of the loads active and reactive power using the previously depicted *ADE7953* integrated circuit.

The *Filter Analysis* block receives the estimated active P and reactive Q power supplied to the load and it provides for each *RC*, the magnitude $M_{f(n)}$ and the phase $\Psi_{(n)}$, that need to be compensated. In fact, $M_{f(n)}$ and $\Psi_{(n)}$ are obtained from
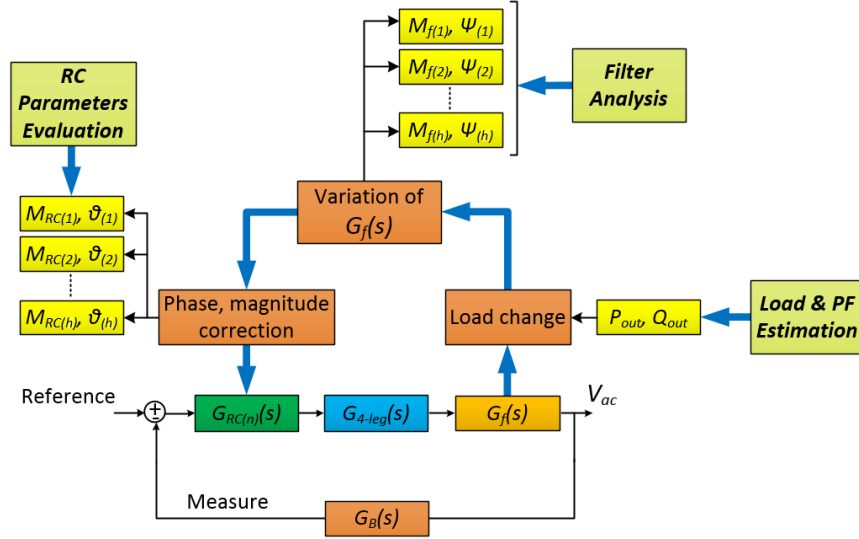
Fig. 12. Blocks scheme of the proposed adaptive control structure.

$G_f(s)$ for the specific frequency where each Resonant Controller is centered. In detail, $M_{f(1)}$ is the magnitude variation introduced by the filter-load system $G_f(s)$, that is required to be compensated at the fundamental frequency (1st order harmonic). Accordingly, $\Psi_{(1)}$ is the phase lagging introduced by $G_f(s)$ at the fundamental frequency, that is compensated properly by the 1st 3D-RC. In general terms, $M_{f(n)}$ and $\Psi_{(n)}$ represent, respectively, the variations of amplitude and phase to compensate and related to the harmonic order n, for the estimated operating point being characterized by the P_{out} and Q_{out} power.

In this manner, the adaptive structure provides the gain and the phase values modification for each 3D-RC, within the control structure, as a function of the active and reactive estimated output power. This allows to compensate for the load-filter interactions of each accounted harmonic up to the order h. The variations in magnitude and phase to compensate for each harmonic, which are included in $G_f(s)$, can be estimated on-line by a simple II order polynomial curve fitting that can be simply implemented even on industrial grade DSP.

Therefore, the load-filter interaction is evaluated accepting a small approximation error against the benefit of a lower computational effort. Considering a general implementation, the inverter and the Butterworth filter are included in the polynomial approximation of the system.

In the *RC Parameter Evaluation* block, each RC structure is modified according to the requirements proving constant behavior in terms of gain and phase shift. For instance, $M_{RC(1)}$ and $\theta_{(1)}$ represent respectively the final corrected gain and the phase of the RC at the fundamental frequency, that are calculated in the operating point having P_{out} and Q_{out}.

Finally, resonant controllers are discretized and the coefficients updated in the Digital Signal Processor (DSP).

Complete system magnitude and phase Bode plots are depicted in Fig. 13, where theoretical results show the effectiveness of the proposed ACS to be used with the introduced resonant controller form. It can be noticed how the system phase is equal to zero at each RCs resonant frequency even in case of load variations. Fig. 14 illustrates a detailed zoom with the purpose to depict the behavior of the high order region implemented RCs. At the RC resonance frequency, which is the most critical point being the gain at its rated value the system is completely compensated.
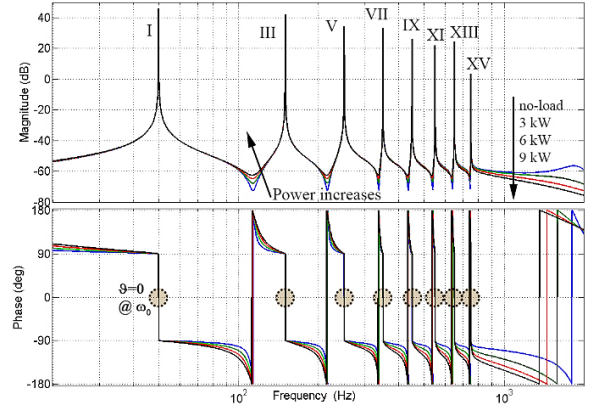

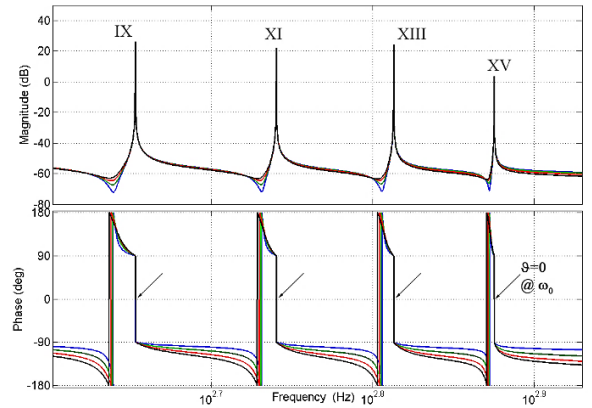Fig. 13. System Bode plots achieved at different load conditions.

Fig. 14. Zoom of Fig. 13 centered at the highest order of the RCs.

V. Experimental Results

The ACS allows compensating up to the 50th harmonic, being able to use 3D-RC of any order up to 50th. Under the same operating conditions, a similar control system, developed without ACS and using RCs up to 9th order has been successfully tested. However, if RCs with an order greater than 11 are employed, the system becomes unstable. The result of a first experimental test of the proposed control strategy, performed at the no-load condition with compensation up to the 15th harmonics, is depicted in Fig. 15, where the steady-state output phase voltages are shown. The steady-state voltage THD is about 0.45% for all the three phase-to-neutral voltages.
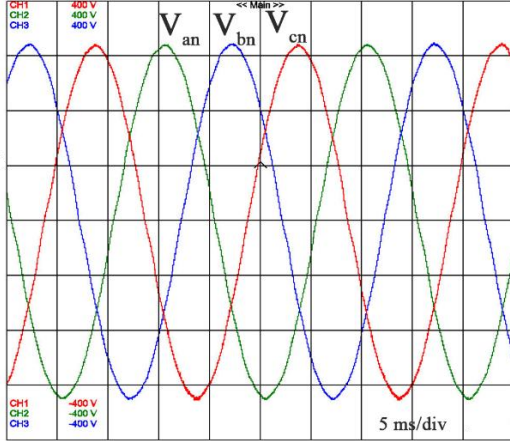

Fig. 15. Inverter output phase voltages when operating at no-load with the auto-tuning algorithm enabled, (100 V/div).

During the test, phase and gain adaptation algorithm was running providing the parameters selected by the initial tuning usually performed at no-load condition, where values of gains and widths are shown in Table II. However, during the transients, the output voltage amplitudes can reach values significantly greater than the steady-state ones yielding to a system instability generated by the highest frequency RCs, namely, the 13th and 15th harmonic compensators. Fig. 16 shows the oscillation at about 750 Hz, of the 15th order RC, that occurs during the transient.
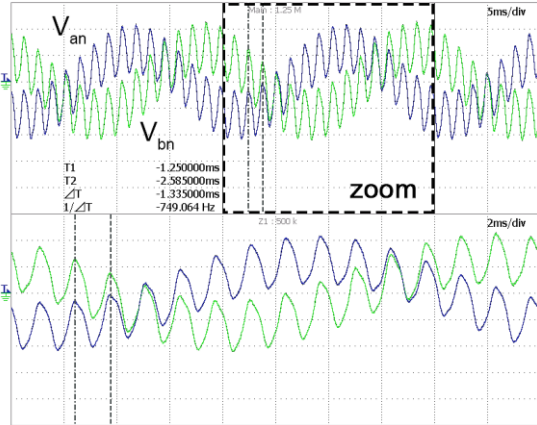

Fig. 16. Output phase voltage 15th harmonic oscillation during the start-up transient. (200 V/div).

The instability of the system is mainly due to the controller discretization that introduces a significant delay in the control loop. To compensate for this delay, an additional term equal to $1.5\omega_{0(n)}T_s$ has been added to the phase ϑ of each RC avoiding the saturation of the regulators. Subsequent tests have been performed, in steady state and transient operating conditions, connecting the inverter to an AC/DC three-phase diode bridge rectifier with filter LC, as shown in Fig. 17.

TABLE II – 3D-RC INITIAL TUNING PARAMETERS

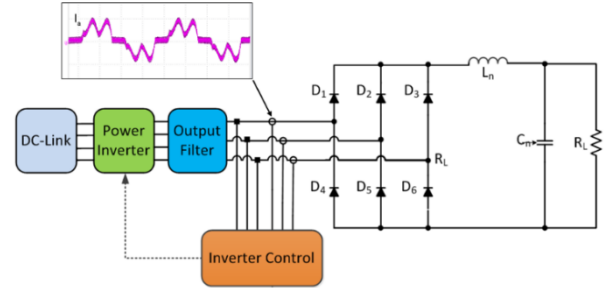| Harmonics	$\omega_0/2\pi$ [s⁻¹]	k_{ir}	ω_{cr} [rad/s]
1	50	130	0.0030
2	100	80	0.0015
3	150	110	0.0020
4	200	60	0.0015
5	250	100	0.0015
6	300	50	0.0015
7	350	100	0.0010
8	400	30	0.0010
9	450	90	0.0010
10	500	45	0.0010
11	550	70	0.0010
12	600	30	0.0010
13	650	50	0.0010
14	700	13	0.0010
15	750	15	0.0009
16	800	11	0.0003
17	850	7	0.0008
18	900	3	0.0003
19	950	5	0.0007
20	1000	1	0.0003
21	1050	3	0.0005
22	1100	1	0.0003
23	1150	3/2	0.0004
24…50	1200…2500	1	0.0003

Fig. 17. Setup for experimental test with 3-phase diodes rectifier load.

In Fig. 18 are shown the output phase voltages V_{an} and V_{bn}, phase current I_a and neutral current I_n, with an equivalent output power around 9 kW, using ACS with 3D-RC odd order up to 15th harmonic. In such a condition the adaptive control algorithm has demonstrated its effectiveness producing a very low phase voltage distortion; in particular, the steady-state voltage THD is equal to about 1.7% on all three phases even if a high distortive load, with a crest factor approximately equal to 3, has been applied. Disabling the adaptive control algorithm, it has been possible to use RCs odd orders up to the 9th harmonic. In this

configuration a steady-state voltage THD equal to about 3.2% for all three phases is achieved.

In order to verify the effectiveness of the control strategy a transient tests, with and without adaptive control algorithm, have been executed, yielding the results depicted in Fig. 19.
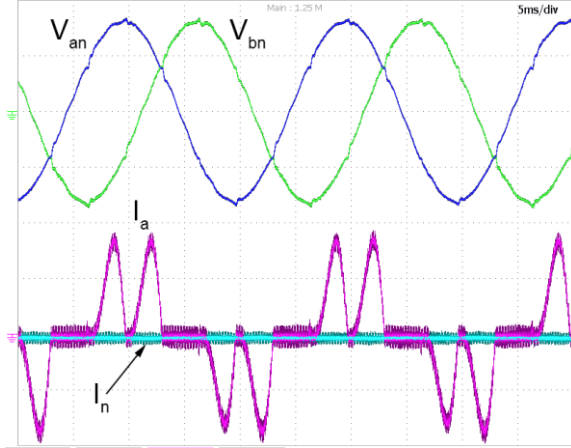

Fig. 18. Voltage (200 V/div) and current (20 A/div) waveforms with a three-phase diode bridge rectifier load. ACS is enabled.
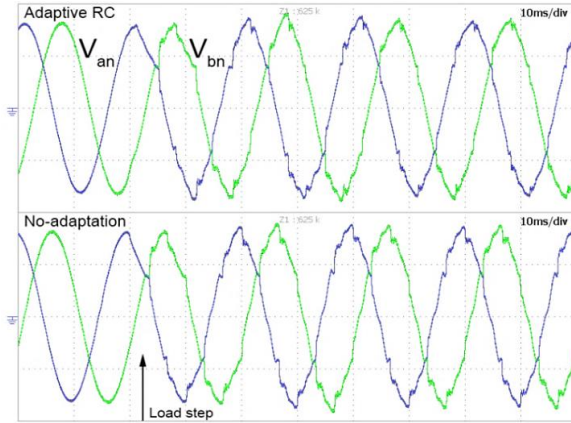

Fig. 19. Transient output phase voltages (200 V/div): comparison between adaptive and standard algorithms for a 9 kW three-phase diode rectifier load.

Comparing the waveforms, it is possible to observe that both the control strategies are able to compensate for the non-linear behavior of the load. However, the harmonics compensation performed by the adaptive control clearly improves the output voltage quality after a couple of periods; on the contrary, the control system without load adaptation does not reach a similar result. This effect is as much marked as output power increases leading, as highlighted above, to the system instability in case of no load adaptation. This problem can be overcome by reducing both the order and gain of the RC, thus reducing the controller accuracy in compensating the harmonics introduced by load, with a consequent increase in voltage THD.

Making the necessary precautions to reduce the truncation and rounding errors on the phase of the discretized system, it has been possible use ACS with 3D-RC up to the 50th

harmonic. Fig. 20 shows the waveforms of the steady-state output phase voltages V_{an} and V_{bn}, obtained with and without load adaptive algorithm, when the VSI is loaded by a 3-phase diode rectifier load having an output power of about 16 kW. The benefit of the ACS clearly appears on the waveform and on the THD values, respectively equal to about 1.7% and to 5.9% on all three phases. The illustrated difference is related to the higher number of resonant controllers included in the multi-RC structure when the proposed load-adaptive algorithm is engaged.
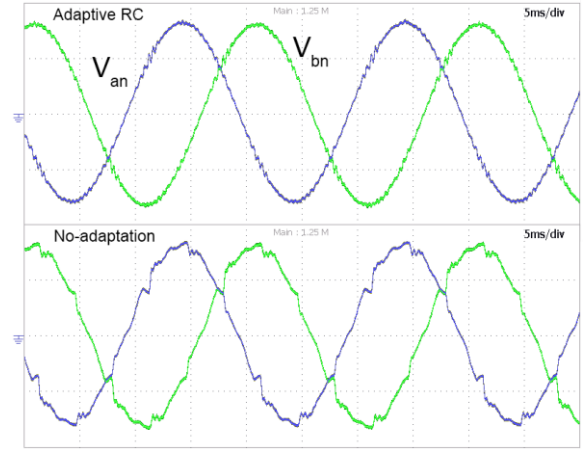

Fig. 20. Steady-state output phase voltages (200 V/div): comparison between adaptive and standard algorithm for a 16 kW three-phase diode rectifier load.

Finally, it is useful to compare the harmonic contents, obtained with the two control strategies, with two international standards, namely EN 50160, relating to the quality of the distribution network and IEC 61000-2-4, concerning the compatibility quality between the distribution network and devices.

Both the harmonic content of the phase voltage V_{an}, obtained with the load adaptation (blue) and without (red), are compared in Fig. 21a to EN 50160 limits and in Fig. 21b to IEC 61000-2-4 ones. It is to notice that the amplitude of the individual harmonics obtained with load adaptation are smaller than no-adaptation load case. The mask obtained by the dotted line delimits the values required by standards. The standard EN 50160 sets limits on the amplitude of single harmonics up to the 25th and voltage THD lesser than or equal to 8%. The IEC 61000-2-4 Class 2 sets limits on the amplitude of single harmonics up to the 50th and voltage THD lesser than or equal to 8%. In some cases the values of the amplitudes obtained without ACS exceed the standards limits, whilst using ACS the system is compliant to both the considered standards.

CONCLUSIONS

A new resonant controller form has been introduced and analyzed. Phase compensated RC is able to provide three degrees of freedom in designing multi-resonant controller based control loops. The presented analysis demonstrates how the RC parameters, as gain, width and phase, can be

selected independently according to the control requirements; furthermore, phase compensation at each resonant frequency allows the usage of different 3D-RC in parallel, improving the stability and accuracy of the system.

An adaptive tuning strategy, based on the output power estimation, has been presented to fully exploit the benefits of the 3D-RC. The proposed control system can be conveniently used in case of supply distorting or loads that are particularly sensitive to voltage variations. The ACS present several advantages such as: improvement of the output voltage quality, excellent system stability and system dynamics independent from the operating point. Finally, the on-line load adaptation algorithm can be applied also to an inverter-based electricity generation systems, having different structures of the filter output power. In fact, the transfer function of the filter can be approximated by the polynomial fitting method, including new values of the RC parameters for adaptation. One possible implementation of this algorithm, for future developments, can also be applied to a grid-connected system, together with a specific grid impedance estimation method.
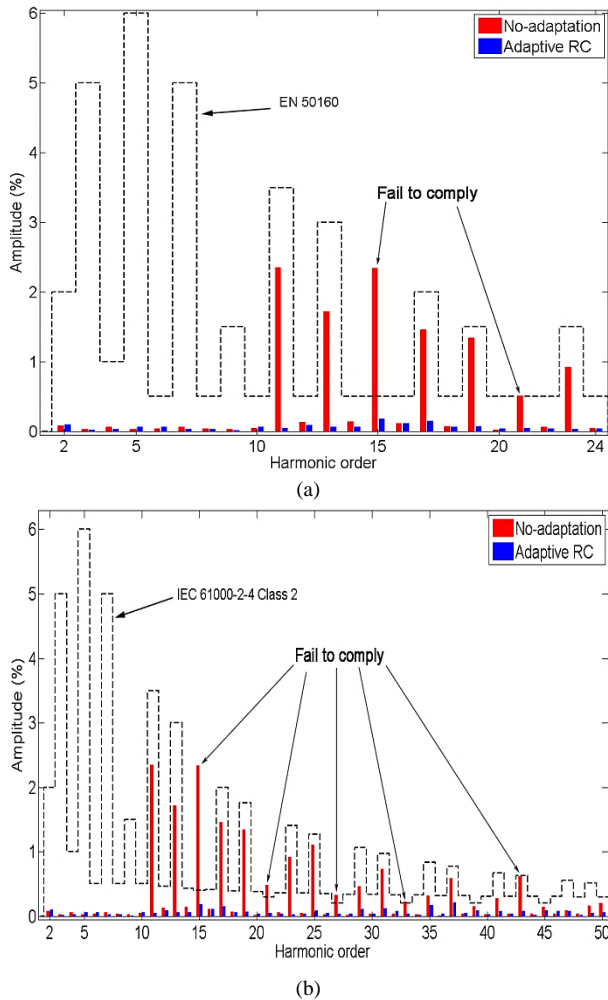

(a)

(b)

Fig 21. Output phase voltage harmonic content obtained with (blue) and without (red) load adaptation algorithm with respect to standard limits: (a) EN 50160; (b) IEC 61000-2-4 Class 2.

REFERENCES

[1] S. Fukuda, R. Imamura, "Application of a sinusoidal internal model to current control of three-phase utility-interface converters", *IEEE Trans. Ind. Electron.*, vol. 52, no. 2, pp. 420-426, April 2005.

[2] M. Mascioli, M. Pahlevani, P.K. Jain, "Frequency-adaptive current controller for grid-connected renewable energy systems", *IEEE 36th International Telecommunications Energy Conference (INTELEC)*, 2014, Sept. 28 2014-Oct. 2 2014.

[3] Shaohua Li, Xiuli Wang, Zhiqing Yao, Tai Li, Zhong Peng, "Circulating Current Suppressing Strategy for MMC-HVDC Based on Nonideal Proportional Resonant Controllers Under Unbalanced Grid Conditions", *IEEE Trans. Power Electron.*, vol. 30, no. 1, pp. 387-397, Jan. 2015.

[4] R. Cárdenas, C. Juri, R. Peña, P. Wheeler, J. Clare, "The Application of Resonant Controllers to Four-Leg Matrix Converters Feeding Unbalanced or Nonlinear Loads", *IEEE Trans. Power Electron.*, vol. 27, no. 3, pp. 1120-1129, March 2012.

[5] Van-Tung Phan, Hong-Hee Lee, "Performance Enhancement of Stand-Alone DFIG Systems With Control of Rotor and Load Side Converters Using Resonant Controllers", *IEEE Trans. Ind. Applicat.*, vol. 48, no. 1, pp. 199-210, Jan.-Feb. 2012.

[6] C. Xia, B. Ji, Y. Yan, "Smooth speed control for low speed high torque permanent magnet synchronous motor using proportional integral resonant controller", *IEEE Trans. Ind. Electron.*, vol. 62, no. 4, pp. 2123-2134, April 2015.

[7] R. Teodorescu, F. Blaabjerg, M. Liserre, P.C. Loh, "Proportional-resonant controllers and filters for grid-connected voltage-source converters", *IEE Proc. Electr. Power Appl.*, vol. 153, no. 5, Sept. 2006.

[8] M. Liserre, R. Teodorescu, F. Blaabjerg, "Multiple harmonics control for three-phase grid converter systems with the use of PI-RES current controller in a rotating frame", *IEEE Trans. Power Electron.*, vol. 21, no. 3, pp. 836-841, May 2006.

[9] A. Timbus, M. Liserre, R. Teodorescu, P. Rodriguez, F. Blaabjerg, "Evaluation of Current Controllers for Distributed Power Generation Systems", *IEEE Trans. Power Electron.*, vol. 24, no. 3, pp. 654-664, March 2009.

[10] Dong Dong, T. Thacker, R. Burgos, Fei Wang, D. Boroyevich, "On Zero Steady-State Error Voltage Control of Single-Phase PWM Inverters With Different Load Types", *IEEE Trans. Power Electron.*, vol. 26, no. 11, pp. 3285-3297, Nov. 2011.

[11] A. Lidozzi, G. Lo Calzo, L. Solero, F. Crescimbini, "Integral-resonant control for stand-alone voltage source inverters", *IET Power Electronics*, vol. 7, no. 2, pp. 271-278, Feb. 2014.

[12] I. Vechiu, O. Curea, and H. Camblong, "Transient operation of a four-leg inverter for autonomous applications with unbalanced load", *IEEE Trans. Power Electron.*, vol. 25, no. 2, pp. 399-407, Feb. 2010.

[13] A.G. Yepes, F.D. Freijedo, O. Lopez, J. Doval-Gandoy, "Analysis and Design of Resonant Current Controllers for Voltage-Source Converters by Means of Nyquist Diagrams and Sensitivity Function", *IEEE Trans. Ind. Electron.*, vol. 58, no. 11, pp. 5231-5250, Nov. 2011.

[14] Yunhu Yang, Keliang Zhou, Ming Cheng, "Phase Compensation Resonant Controller for PWM Converters", *IEEE Trans. Ind. Informat.*, vol. 9, no. 2, pp. 957, 964, May 2013.

[15] A. G. Yepes, F. D. Freijedo, J. Doval-Gandoy, O. Lopez, J. Malvar, P. Fernandez-Comesana, "Effects of Discretization Methods on the Performance of Resonant Controllers", *IEEE Trans. Power Electron.*, vol. 25, no. 7, pp. 1692-1712, July 2010.

[16] A. G. Yepes, F. D. Freijedo, O. Lopez, J. Doval-Gandoy, "High-Performance Digital Resonant Controllers Implemented With Two Integrators", *IEEE Trans. Power Electron.*, vol. 26, no. 2, pp. 563-576, Feb. 2011.

[17] S.A. Khajehoddin, M. Karimi-Ghartemani, P.K. Jain, A. Bakhshai, "A Resonant Controller With High Structural Robustness for Fixed-Point Digital Implementations", *IEEE Trans. Power Electron.*, vol. 27, no. 7, pp. 3352,3362, July 2012.

[18] G. Lo Calzo, A. Lidozzi, L. Solero, F. Crescimbini, "LC Filter Design for On-grid and Off-grid Distributed Generating Units", *IEEE Trans. Ind. Applicat.*, vol. 51, no. 2, pp. 1639-1650, March-April 2015.

[19] A Nabae, T. Tanaka, "A new definition of instantaneous active-reactive current and power based on instantaneous space vectors on polar coordinates in three-phase circuits", *IEEE Trans. Power Deliv.,* vol. 11, no. 3, pp. 1238-1243, July 1996.

[20] R.S. Herrera, P. Salmeron, J.R. Vazquez, S.P. Litran, A. Perez, "Generalized instantaneous reactive power theory in poly-phase power systems", *EPE'09 13th European Conference on Power Electronics and Applications*, 8-10 Sept. 2009.

[21] M. Depenbrock, V. Staudt, H. Wrede, "A theoretical investigation of original and modified instantaneous power theory applied to four-wire systems", *IEEE Trans. Ind. Applicat.*, vol. 39, no. 4, pp. 1160-1168, July-Aug. 2003.